An empirical model (CH-Therm-2018) of the thermospheric mass density derived from CHAMP

Chao Xiong[1], Hermann Lühr[1], Michael Schmidt[2], Mathis Bloßfeld[2], and Sergei Rudenko[2]

[1]GFZ German Research Centre for Geosciences, Telegrafenberg,14473 Potsdam, Germany
[2]Deutsches Geodätisches Forschungsinstitut at the Technische Universität München (DGFI-TUM), Arcisstr. 21, 80333 Munich, Germany

Correspondence to: Xiong C. (bear@gfz-potsdam.de)

Abstract. Thermospheric drag is the major non-gravitational perturbation acting on Low Earth Orbit (LEO) satellites at altitudes up to 1000 km. The drag depends on the thermospheric density, which is a key parameter in the planning of LEO missions, e.g. their lifetime, collision avoidance, precise orbit determination, as well as orbit and re-entry prediction. In this study, we present an empirical model, named CH-Therm-2018, of the thermospheric mass density derived from 9-year (from

5   August 2000 to July 2009) accelerometer measurements at altitude from 460 to 310 km, from the CHAllenging Minisatellite Payload (CHAMP) satellite. The CHAMP dataset is divided into two 5-year periods with 1-year overlap (from August 2000 to July 2005 and from August 2004 to July 2009) to represent the high-to-moderate and moderate-to-low solar activity conditions, respectively. The CH-Therm-2018 model describes the thermospheric density as a function of seven key parameters, namely, the height, solar flux index, season (day of year), magnetic local time, geographic latitude and longitude, as well as mag-

10   netic activity represented by the solar wind merging electric field. Predictions of the CH-Therm-2018 model agree well with the CHAMP observations (disagreements within ±20%), and show different features of thermospheric mass density during solar activities, e.g. the March-September equinox asymmetry and the longitudinal wave pattern. We compare the CH-Therm-2018 predictions with the Naval Research Laboratory Mass Spectrometer Incoherent Scatter Radar Extended (NRLMSISE-00) model. The result shows that CH-Therm-2018 better predicts the density evolution during the last solar minimum (2008-2009)

15   than the NRLMSISE-00 model. From the analysis of Satellite Laser Ranging (SLR) observations of the ANDE-Pollux satellite during August-September 2009, we estimate 6-hour scaling factors of the thermospheric mass density provided by our model and obtain their median value equal to 1.27±0.60 indicating that our model, on average, slightly underestimates the thermospheric mass density at the solar minimum.

20   # 1   Introduction

The thermosphere is the top layer of the gravitationally bound part of atmosphere, which is partly ionized and extends from about 90 km to over 600 km (Lühr et al., 2004). Its density variations are mainly driven by the extreme solar ultraviolet (EUV)

irradiation, energetic particle precipitation and electrical energy from the magnetosphere and solar wind, as well as by waves originating in the lower atmosphere that propagate upward into the thermosphere. The thermospheric mass density in general falls off exponentially with increasing altitude, with scale heights of about 25 km to 75 km in the upper atmosphere, depending on altitude and solar flux levels. In addition to the vertical variation, the mass density varies also horizontally (latitude and

5   longitude) and with solar flux, geomagnetic activity, season and local time (Emmert, 2015).

The thermosphere plays a crucial role for the near-Earth space operations, as the total mass density is the key parameter for orbit perturbation of low Earth orbit (LEO) satellites. Therefore, knowledge of the thermospheric density is critical in the planning of LEO missions, such as their orbital altitudes, lifetime, and re-entry prediction. As the ionosphere is embedded in the thermosphere, the knowledge of thermospheric density will also help to improve our understanding of the coupling between

10   thermosphere, ionosphere and lower-atmosphere (Liu et al., 2013; Emmert, 2015).

There are several tools for measuring the thermospheric mass density. The atmospheric drag provides the most direct means, which can be measured by the onboard accelerometers (e.g., Champion and Marcos, 1973; Lühr et al., 2004; Doornbos et al., 2010) or estimated from the changes of the LEO's trajectory (e.g., King-Hele, 1987; Emmert at al., 2004). Other instruments, such as neutral mass spectrometers (e.g., Von Zahn, 1970; Hedin, 1983), ultraviolet remote sensing (e.g., Meier and Picone,

15   1994; Christensen et al., 2003), as well as the pressure gauge mounted on the rockets (e.g., The Rocket Panel, 1952; Clemmons et al., 2008), can also be used for inferring the mass density. The details of these techniques have been reviewed by several earlier studies (e.g., Osborne et al., 2011; Clemmons et al., 2008; Emmert, 2015). Various empirical models have also been proposed to describe the thermospheric mass density variability. The most widely used are the Mass Spectrometer Incoherent Scatter Radar Extended (MSISE) model (Hedin, 1991; Picone et al., 2002), the Drag Temperature Model (Bruinsma et al.,

20   2003, 2012) and the Jacchia-Bowman 2008 (JB2008) model series (Bowman et al., 2008a; Bowman et al., 2008c). Liu et al. (2013) and Yamazaki et al. (2015) reported two empirical models derived from recent LEO missions, such as the CHAllenging Minisatellite Payload (CHAMP, Reigber et al. (2002)) and the Gravity Recovery and Climate Experiment (GRACE, Tapley et al. (2004)). These two models can well represent the prominent thermospheric structures at low latitude like the equatorial mass density anomaly (EMA) and the wave-4 longitudinal pattern, as well as the solar wind influence on the high latitude

25   thermosphere, respectively.

As reported by previous studies, the height and solar activity are the two important factors that affect the thermosphere mass density (Liu, 2005; Guo et al., 2008; Lei et al., 2012). The CHAMP altitude decreased coincidentally within the declining phase of solar cycle 23/24, therefore, it is difficult to fully separate the height and solar activity effects on mass density from CHAMP observations. By assuming a linear dependence on height variation, Liu et al. (2013) used the dataset from 2002 to

30   2005 when CHAMP was at the altitude of 420 km to 350 km to construct the model, focusing on low- and mid-latitudes. The authors argued that a linear approximation is applicable within an error of about 3.5 % over one scale height. To reduce the height variation effects on the model, Yamazaki et al. (2015) used the MSISE-00 model to normalize the CHAMP and GRACE densities to a common height of 450 km, focusing on high latitudes. However, as the MSISE-00 model was not accurate during the extreme solar minimum of 2008 to 2009 (Thayer et al., 2012; Liu et al., 2014a), it would possibly affect

35   their height correction during the solar minimum period, therefore, they used also the dataset from 2002 to 2006. Both models

above considered only the dataset from high to moderate solar activity, while the dataset from the solar minimum (2008 to 2009) has not been included.

To make more efficiently use of the CHAMP observation, we consider in this study the dataset from August 2000 to July 2009 for constructing empirical models of the thermospheric mass density, to see if there are different features at high and low

5 solar activities. The rest of the paper is organized as follows. In Sect. 2, we first briefly introduce the CHAMP satellite and its accelerometer measurements, describe our model construction approach and present the CH-Therm-2018 itself. Our model predictions and the comparison with other models are given in Sect. 3. Section 4 presents a validation of our model using Satellite Laser Ranging (SLR) measurements to the spherical satellite ANDE-Pollux. In Sect. 5 we provide relevant discussion and summarize the main findings.

10 ## 2   Data and Model Construction

2.1   CHAMP satellite and its accelerometer measurements

The CHAMP spacecraft was launched on July 15, 2000 into a near-circular polar orbit (inclination: $87.3°$) with an initial altitude of 456 km. By the end of the mission, September 19, 2010, the orbit had decayed to about 250 km. For covering all local times once, CHAMP needed 131 days. The thermospheric mass density measurements were deduced from the on

15 board accelerometer, which aimed to measure the non-conservative forces exerted on the satellite with a resolution of less than 10^{-9} ms^{-2} in along-track and cross-track directions (Reigber et al., 2002). The basic equations for deriving the thermospheric mass density from accelerometer measurements have been described in Lühr et al. (2004) and Liu (2005), and by means of an improved approach the mass density is provided with a resolution of less than 10^{-14}kg/m^3 (Doornbos et al., 2010).

2.2   Our approach for constructing the CH-Therm-2018 empirical model

20 To give an overview of the CHAMP mission, Fig. 1 (top panel) shows the satellite altitude variations for the whole mission period. Its mean value decayed from about 460 km in July 2000 to 260 km in September 2010. We see that the satellite was lifted four times (twice in 2002, once in 2006 and 2009) to higher altitude where the air drag is smaller, for extending the lifetime. The thermospheric mass density derived from the on-board accelerometer is presented in the bottom panel, which shows decreasing density from 2002 to 2009, coinciding with the reducing solar flux. But from August 2009 to the end of

25 mission, the derived mass density has increased dramatically from about $5 \cdot 10^{-12}$ to $40 \cdot 10^{-12}$ kg/m^3, which is mainly caused by the rapid decrease in satellite altitude during the last mission year.

In CH-Therm-2018, we consider an exponential function with a constant scale height for describing the height variation of the thermosphere mass density. However, as seen in Fig. 1, the CHAMP-measured density has dramatically increased by almost a factor of 8 when its altitude goes below 310 km, which also indicates that using a constant scale height is not suitable

30 over the whole altitude range from 250 km to 460 km, especially for the lowest parts. Therefore, in this study we consider a 9-year dataset from August 2000 to July 2009 when the satellite was above 310 km, and divide the dataset into two 5-year
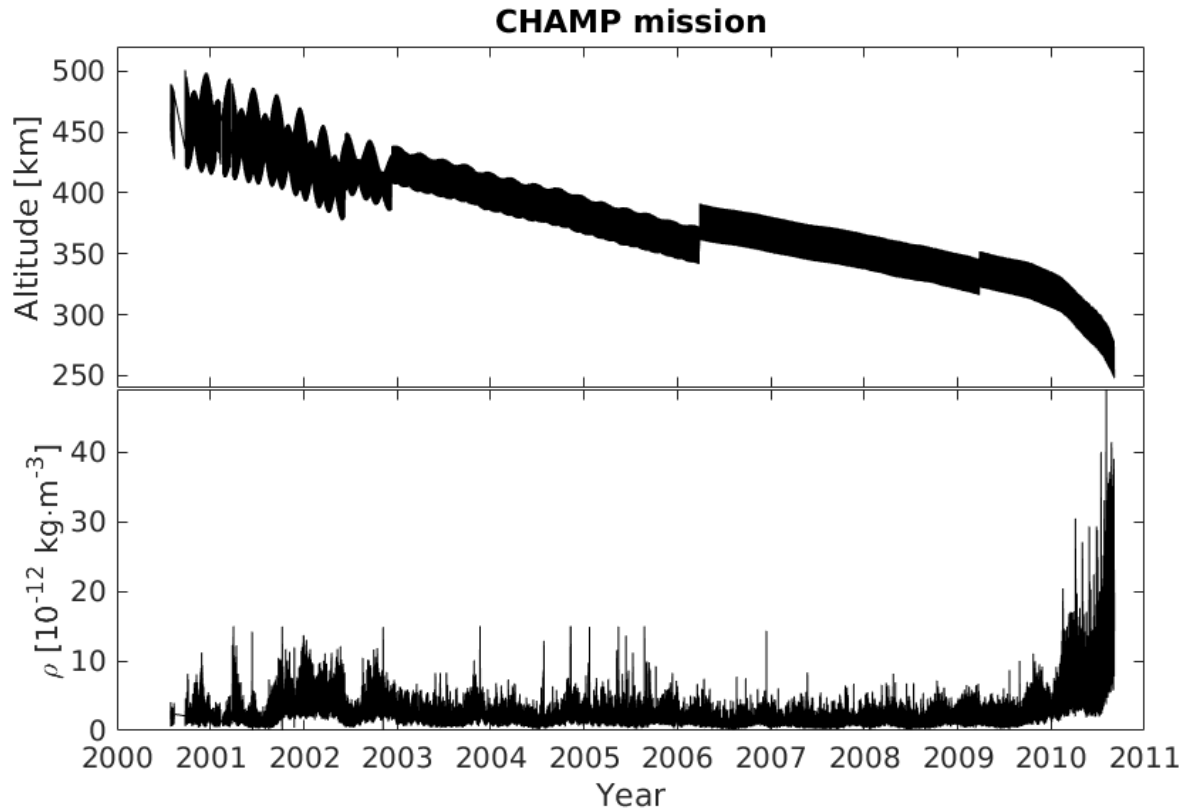
Figure 1. The satellite altitude (top) and thermospheric mass density (bottom) measured by CHAMP for the whole mission period.

periods with 1-year overlap, for representing the high-to-moderate and moderate-to-low solar activity conditions. The altitude of CHAMP decayed from about 460 km to 370 km and from 390 km to 310 km during the two periods, respectively.

According to Guo et al. (2008), the solar flux index P10.7 is more suitable than F10.7 to represent thermospheric mass density variations. P10.7 is defined as $P10.7 = (F10.7 + F10.7A)/2$, where F10.7A is the 81-day averaged value of daily

5 F10.7. Figure 2 (top panel) shows the P10.7 variations from 2000 to the end of 2010, which decrease from over 250 SFU (Solar Flux Unit) in 2002 to below 70 SFU in 2008-2009, and then slightly increased back to 75 SFU at the end 2010. The mean values of P10.7 during the considered two 5-year periods hereafter referred to as $P10.7_{ref}$ are 144.7 and 79.7 SFU, respectively. The bottom panel in Fig. 2 shows the variations of solar wind merging electric field, E_m. Liu et al. (2010, 2011) and Zhou et al. (2013) found that E_m is an appropriate parameter to describe the disturbance of the thermospheric mass density
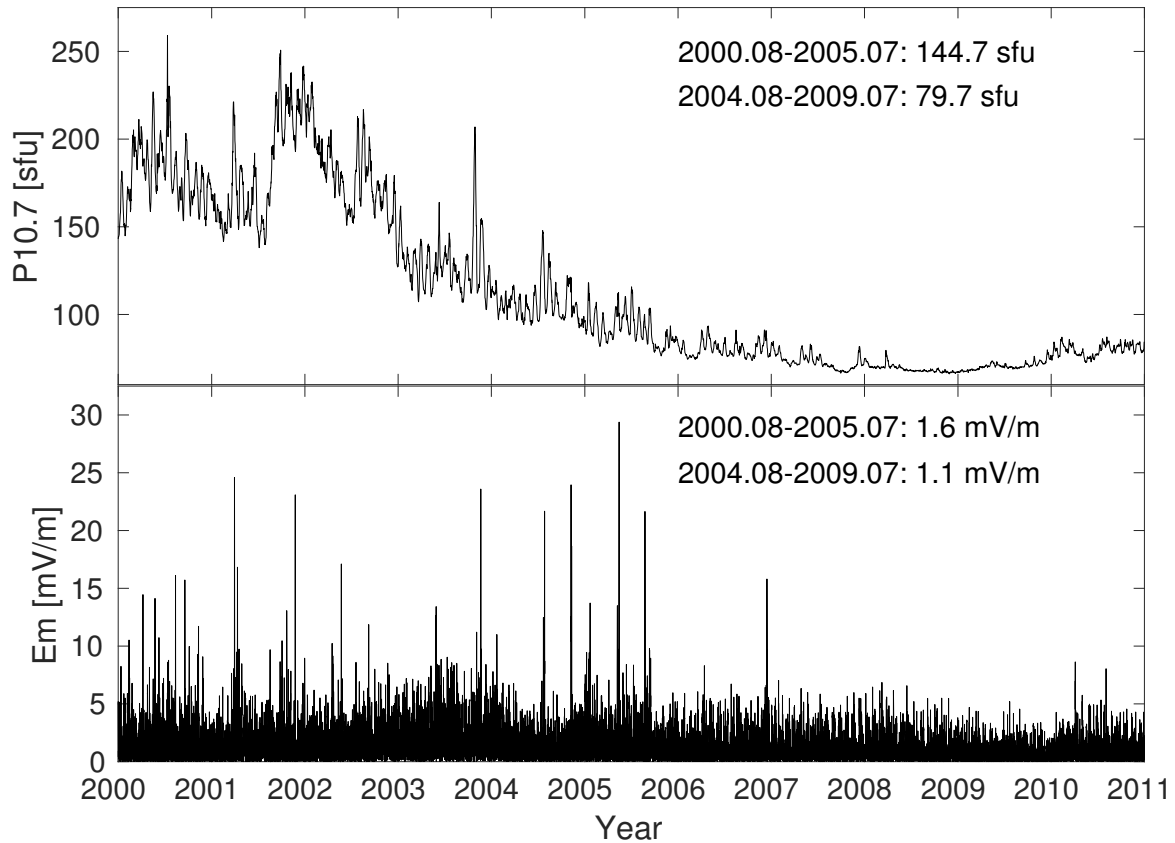
Figure 2. The variations of the solar flux index (P10.7, top) and solar wind merging electric field (E_m, bottom) from 2000 to 2010. The mean values of two parameters during two 5-year periods (from August 2000 to July 2005 and from August 2004 to July 2009), P10.7$_{\text{ref}}$ and $E_{m_{\text{ref}}}$, respectively, are given in the upper part of each panel.

at increased magnetic activities. Considering the memory effect of the magnetosphere-ionosphere-thermosphere system to a solar wind input (Werner and Prölss, 1997; Liu et al., 2010), E_m can be defined as:

$$E_m(t,\tau) = \frac{\int_{t_1}^{t} E_m'(t')e^{(t'-t)/\tau}\mathrm{d}t'}{\int_{t_1}^{t} e^{(t'-t)/\tau}\mathrm{d}t'}, \tag{1}$$

where E_m' represents a continuous function of time t' of the actual merging electric field. t_1 is a time chosen to be 3 hours

5   before the actual epoch (t), and τ, here 0.5 h, is the e-folding time of the weighting function in the integrands. For calculating

E'_m, we use the solar wind-to-magnetosphere coupling functions as defined by Newell et al. (2007), and to make E'_m values comparable with the solar wind electric field, the function has been rescaled as:

$$E'_m = \frac{1}{3000} V_{\text{SW}}^{\frac{4}{3}} (\sqrt{B_y^2 + B_z^2})^{\frac{2}{3}} \sin^{\frac{8}{3}}(\frac{\Theta}{2}), \tag{2}$$

where V_{SW} is the solar wind velocity in km/s, and both B_y and B_z (in nT) are the interplanetary magnetic field (IMF) compo-
5   nents in Geocentric solar magnetospheric (GSM) coordinates, Θ is the clock angle of the IMF ($\tan \Theta = |B_y|/B_z$). With these units, the value of the merging electric field will result in mV/m. This approach for calculating the merging electric field has also been used by Xiong and Lühr (2014) and Xiong et al. (2016). From Fig. 2, we see that the values of the merging electric field are below 5 mV/m during most of the time (slightly higher during higher solar activity years), with mean values hereafter referred to as $E_{m_{\text{ref}}}$ of 1.6 and 1.1 mV/m for the two 5-year periods, respectively.

10   For constructing the empirical model, we consider the dependences on height (h) measured in km, solar flux (P10.7), season (DoY, day of year), magnetic local time (MLT), geographic latitude (Θ) measured from $-90°$ (south pole) to $90°$ (north pole) and longitude (ϕ), and magnetic activity (E_m). Similar to Marinov et al. (2004) and Liu et al. (2013), we use the multivariable least-square fitting for deriving the coefficient matrix of the CHAMP measurements, which is expressed as:

$$\begin{aligned} \rho = &f_1(\rho_0, h, H_d) \cdot f_2(\text{P10.7}) \cdot f_3(\text{DoY}) \cdot f_4(\text{MLT}) \\ &\cdot f_5(\Theta) \cdot f_6(\phi) \cdot f_7(E_m), \end{aligned} \tag{3}$$

15   where ρ is the model predicted mass density, ρ_0 is the mass density (10^{-12} kg/m^3) at the reference height (310 km, the lowest height of CHAMP during the considered 9-year period), and H_d denotes the mass density scale height (km). The seven

sub-functions are defined as:

$$f_1(\rho_0, h, H_d) = \rho_0 \cdot e^{(-(h-310)/H_d)}, \tag{4}$$

$$f_2(\text{P10.7}) = a_0 + a_1 \cdot (\text{P10.7} - \text{P10.7}_{\text{ref}}) + \\ a_2 \cdot (\text{P10.7} - \text{P10.7}_{\text{ref}})^2, \tag{5}$$

$$f_3(\text{DoY}) = b_0 + \sum_{i=1}^{3}\{b_1(i) \cdot \cos(\frac{i \cdot 2\pi \cdot \text{DoY}}{365.25}) + \\ b_2(i) \cdot \sin(\frac{i \cdot 2\pi \cdot \text{DoY}}{365.25})\}, \tag{6}$$

$$f_4(\text{MLT}) = c_0 + \sum_{j=1}^{4}\{c_1(j) \cdot \cos(\frac{j \cdot 2\pi \cdot \text{MLT}}{24}) + \\ c_2(i) \cdot \sin(\frac{j \cdot 2\pi \cdot \text{MLT}}{24})\}, \tag{7}$$

$$f_5(\Theta) = d_0 + \sum_{k=1}^{6}\{d_1(k) \cdot \cos(\frac{k \cdot 2\pi \cdot \Theta}{180}) + \\ d_2(k) \cdot \sin(\frac{k \cdot 2\pi \cdot \Theta}{180})\}, \tag{8}$$

$$f_6(\phi) = g_0 + \sum_{l=1}^{4}\{g_1(l) \cdot \cos(\frac{l \cdot 2\pi \cdot \phi}{360}) + \\ g_2(l) \cdot \sin(\frac{l \cdot 2\pi \cdot \phi}{360})\}, \tag{9}$$

$$f_7(E_m) = m_0 + m_1 \cdot (E_m - E_{m_{\text{ref}}}) + \\ m_2 \cdot (E_m - E_{m_{\text{ref}}})^2. \tag{10}$$

The height variation of mass density is described by an exponential function, i.e. Eq. (4), and normalized to the altitude at 310 km. To better use the linear and quadratic fitting, P10.7 and E_m have been normalized to their mean values of each 5-year period, as seen in Eqs. (5) and (10). The dependences of the other parameters, such as season, magnetic local time, geographic latitude and longitude, have been approximated by trigonometric functions considering harmonics from 3 to 6-orders, as shown from the Eqs. (6) to (9). In this way, 46 parameters are needed to construct the model and all the bias values in the Eqs. (6) to (9), namely b_0, c_0, d_0, and g_0, have been set to 1.0.

3 CH-Therm-2018 model results and comparison with other empirical models

As described above, by using each 5-year period of CHAMP measurements we have derived empirical models based on 46 free parameters for the high and low solar activity periods, respectively. The values of these parameters are listed in Table 1. In the following we are going to compare the main features captured by our models for different solar activity conditions.

The panels (a) and (b) of Fig. 3 present the altitude versus solar activity variations during the two periods, over an altitude range from 310 to 470 km. As the level of the solar activity is quite different for the two periods, the range of P10.7 has been

limited to 100-280 SFU and 65-125 SFU, respectively. The model predicted mass density shows generally similar variations
for both periods, which increases with larger solar activity but decreases with altitude. The borders between different colors can
be interpreted as constant pressure levels. Panels (c) and (d) of Fig. 3 show the altitude versus geographic latitude variations
of the mass density around noon. The P10.7 values for the two periods have been set to 150 and 80 SFU, respectively. The

5   mass density generally decreases from low to high latitudes during both periods. For the higher solar activity condition, the
equatorial mass density anomaly (EMA) can clearly be seen, with the peak mass density appearing around $\pm 20°$ latitude. And
for the lower solar activity condition, a density trough is seen at high latitudes (around $\pm 70°$), which is more evident in the
southern hemisphere. The panels (e) and (f) of Fig. 3 show the dependence of our model-predicted mass density on merging
electric field during both periods. We see that the mass density roughly linearly denpendes on the merging electric field, with

10   almost the same slopes for both periods.

The panels (a) and (b) of Fig. 4 present the MLT versus latitude distribution of the mass density. The solar activity has been
set again to 150 and 80 SFU for the two periods and the altitude has been set to 400 and 340 km, respectively. During both
solar activity periods, the mass density reaches it maximum and minimum around 14 h MLT and 3 h MLT, respectively. The
EMA feature is more evident at higher solar activity conditions, as shown in panel (a) of Fig. 4, with larger crest density in the

15   northern hemisphere as we have chosen the September equinox. Additionally, a clear density trough is seen around $-75°$ in
the southern hemisphere during the lower solar activity condition. The panels (c) and (d) of Fig. 4 present the seasonal versus
latitude variations of the thermospheric mass density, showing mass density peaks at the two equinox seasons and a minimum
around the June solstice. An interesting feature is that the mass density exhibits larger amplitudes during the March equinox
than during the September equinox for high solar activity condition, while it exhibits an opposite sense for lower solar activity

20   condition. This equinox asymmetry of thermospheric mass density is consistent with the findings of Liu et al. (2013), who
reported that the equinox asymmetry weakens or disappears when the solar flux level falls to below P10.7 = 110 SFU. Guo et
al. (2008) argued that the March-September equinox asymmetry can be partly attributed to the inter-annual variability of the
thermosphere mass density.

The coupling between the lower atmosphere and upper atmosphere/ionosphere have been widely reported by the longitudinal

25   wave patterns of different thermospheric/ionospheric parameters (e.g., Immel et al., 2006; Häusler et al., 2007; Liu et al.,
2009). The tides excited by latent heat release in tropospheric deep convective tropical clouds can propagate vertically upward
(Hagan and Forbes, 2003). These tides vary differently with season, causing the thermospheric/ionospheric quantities to show
longitudinal patterns with varying wave numbers over the course of a year. Best known are the wave number-4 (WN4) patterns
during the months around August and wave number-3 (WN3) pattern around solstice seasons, corresponding to the diurnal

30   eastward propagating wave-3 (DE3) and wave-2 (DE2) nonmigrating tides, respectively (e.g., Immel et al., 2006; Lühr et al.,
2008; Wan et al., 2010). The panels (e) and (f) of Fig. 4 show the global distribution around the noon time of the mass density
at 400 and 340 km altitude, for P10.7 equal to 150 and 80 SFU, respectively. Here we find again the EMA feature. Some tidal
features, a mixture of longitudinal wave-3 and wave-4 patterns, are found at EMA crest regions during the higher solar activity
conditions. While for the lower solar activity, the wave-2 and wave-3 is more prominent. These different longitudinal wave

35   patterns may result from the different contributions of the lower atmosphere tidal forcing to the upper atmosphere, due to their
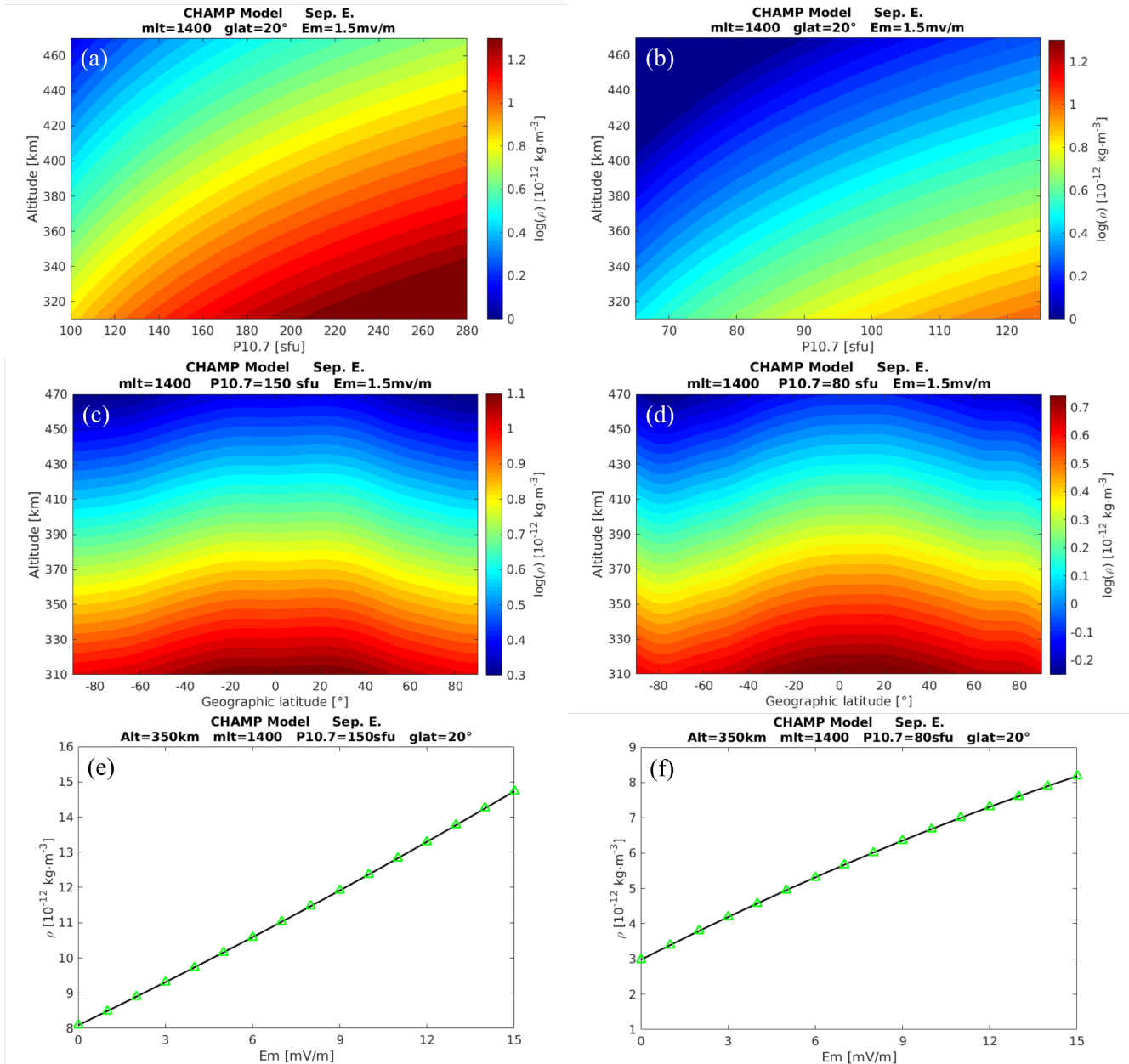
Figure 3. The altitude versus solar activity variations of the model-predicted thermospheric mass density around noon at (a) high and (b) low solar activity conditions. The longitude has been chosen at Greenwich meridian. (c) and (d) show the altitude versus geographic latitude variations of the model-predicted mass density for high and low solar activity conditions, respectively. (e) and (f) show the dependence of the model-predicted mass density on merging electric field for both periods.
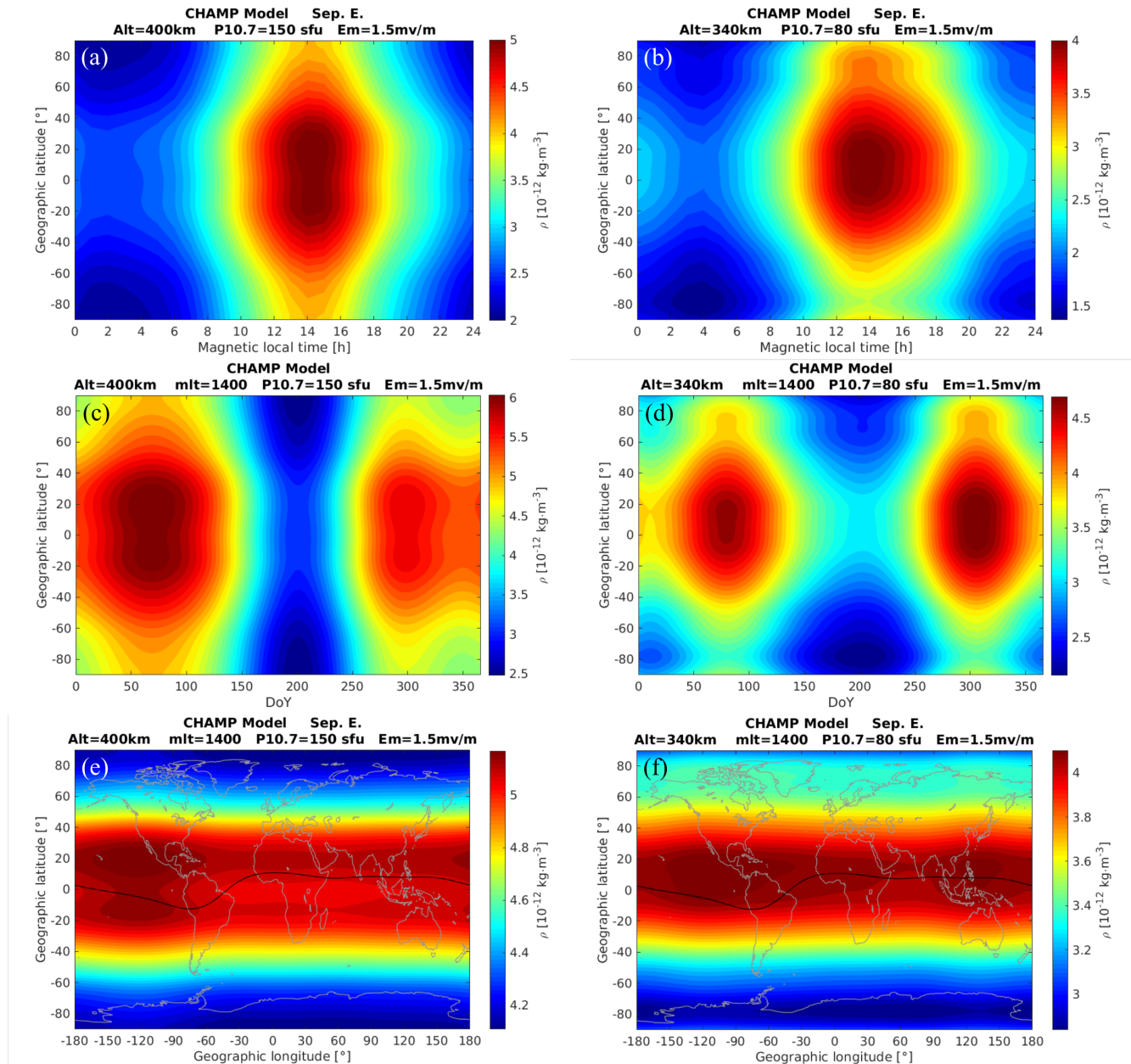
Figure 4. Similar as Fig. 3, but for the distribution of (a) and (b): geographic latitude versus magnetic local time; (c) and (d): geographic latitude versus day of year; (e) and (f): geographic latitude versus longitude.

different wavelengths and relative susceptibility to the molecular dissipation at different solar flux conditions (Bruinsma and Forbes, 2010).

For reproducing the CHAMP observations with our empirical model, we have combined the results derived from both periods. For the results from August 2000 to July 2004, we use the model predictions from the first 5-year period, while for the results from August 2005 to July 2009, we use the model predictions from the second 5-year periods. For the one-year overlapping period from August 2004 to July 2005, we consider the model predictions from both periods, but use a

5 linear-weighted combination for the time of overlap. Fig. 5 (top panel) presents our model predictions (red) and CHAMP observations (black) from August 2000 to July 2009. In general, our model follows quite well the measurements, and even the spikes (corresponding to higher magnetic activity) are reasonably well reproduced. For the comparison, the mid panel shows also the result from the NRLMSISE-00 model (green). Compared to our model, the NRLMSISE-00 model is clearly overestimating the CHAMP observation during solar minimum years. The bottom panel presents quantitatively the relative

10 differences between the model predictions and CHAMP observations:

$$\Delta\rho = \frac{\rho_{\mathrm{model}} - \rho_{\mathrm{CHAMP}}}{\rho_{\mathrm{CHAMP}}}. \tag{11}$$

The annual average differences between our model and observations are below ± 20 % for all nine years, while NRLMSISE-00 overestimates the observations by about 30 % for high and moderate solar activity years, and reaches as high as 80 % for the extremely low solar activity years. It is no surprise that our model predicts better than the NRLMSISE-00 model, because our

15 model is derived from CHAMP observations, which have not been included in the NRLMSISE-00 model. Anyhow, Fig. 5 demonstrates that our model can reproduce the CHAMP observations fairly well.

For a more quantitative inspection of the CHAMP model, we have divided the 9-year dataset into 2-month bins of overlapping 131-day intervals for covering all 24-hour local times in each bin. For the 2-month bins, we calculate the linear regression slope and the mean ratio between the CHAMP observations and model predictions. The mean ratio is defined as the ratio

20 between the mean values of the observations divided by the model predictions during the 131 days. Examples of this analysis during high (centered on March 1, 2002) and low (November 1, 2008) solar activities are presented in Fig. 6 (a) and (b), respectively. The correlation coefficients between the model predictions and observations reach 0.89 and 0.86, the slopes of the linear fitting are 1.03 and 1.07, and the mean ratios are 1.11 and 1.04. Panel (c) of Fig. 6 presents the slope (top panel) and mean ratio (bottom panel) between the observations and our empirical model (red), as well as the NRLMSISE-00 model

25 (green), respectively.

The slope of the CHAMP model results varies within the range of 0.75 to 1.2 and the mean ratio varies between 0.9 and 1.15 during almost all the nine years, both of which are better than those of the NRLMSISE-00 model. An exception is the values of slopes reaching as low as 0.55 around the end of 2003, which means both our and NRLMSISE-00 models overestimate the mass density. These deviations can be attributed to overestimations by the models in October and November 2003 (see Fig. 1)

30 during the periods of very strong magnetic storms.

It is worth to note that we have extended the model prediction to the last year of the CHAMP mission, as shown in Fig. 6 (c). We see that the slope and the mean ratio between observations and our empirical model have increased dramatically, reaching the values of over 4.0 and 2.0 at the end of the mission, respectively. This is a consequence of the quite low altitude of the
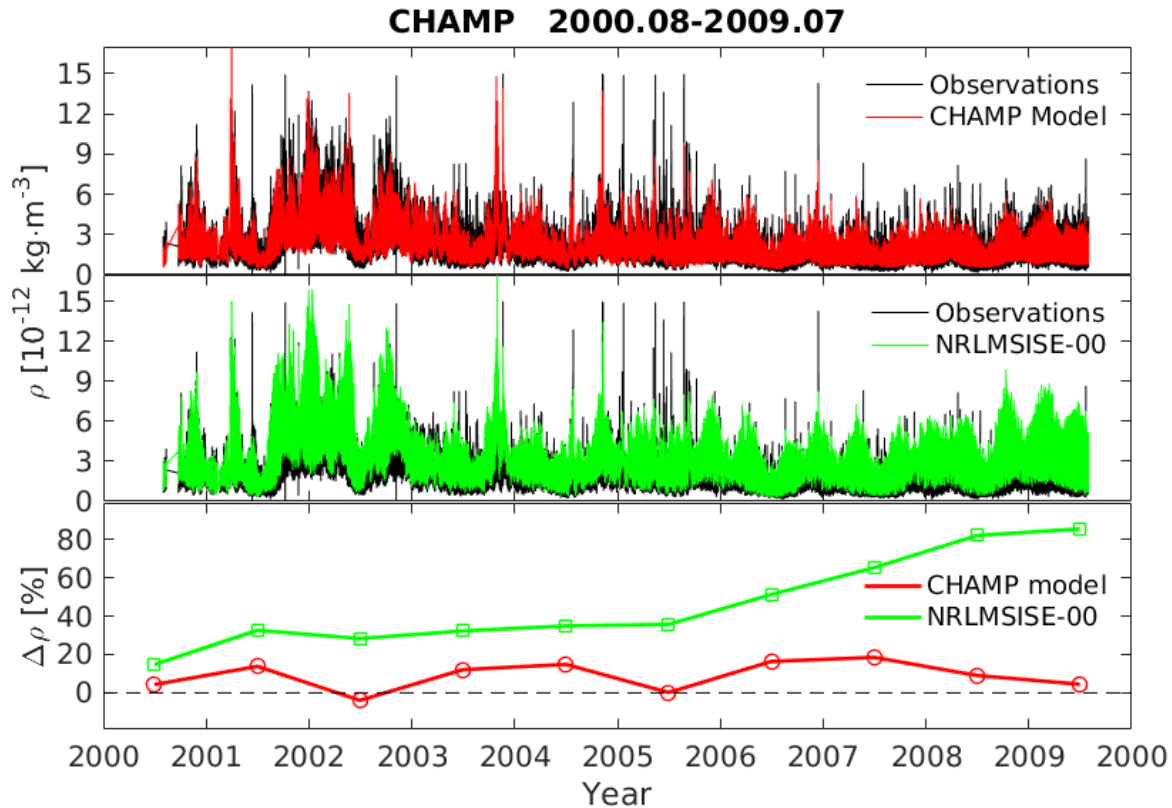
Figure 5. The upper panel shows the predicted thermospheric mass density (red) and CHAMP observations (black) from August 2000 to July 2009. The mid panel shows the same density but for the NRLMSISE-00 model (green) and CHAMP observations (black). The lower panel gives the annual average relative differences between the model estimates and CHAMP observations.

CHAMP satellite. Therefore, we have to note that our model is suitable for the altitude range from 310 to 470 km. And the large increase of the CHAMP-measured mass density during the last mission year (see Fig. 1) might be an indication of a smaller scale height due to a composition change at altitudes below 310 km.

4 Validation with SLR measurements

5 Atmospheric drag is the major non-gravitational perturbation acting on LEO satellites and causes an orbital decay. Since the atmospheric drag depends, among other parameters on the thermospheric density, SLR measurements of spherical LEO satellites can be used to estimate scaling factors for the density derived from various empirical models and, therefore, either validate them or provide corrections to these models (Panzetta et al., submitted). This is not an easy task, since, on the one hand, it requires precise modeling of all other gravitational and non-gravitational perturbations acting on the satellites, and on

10 the other hand, the amount of SLR observations to LEO satellites is low.

As an example, from the analysis of SLR observations to the cannon-ball LEO satellite ANDE-Pollux between August 16 and October 3, 2009, (Panzetta et al., submitted) derived 6-hour time series of the scaling factors of the thermospheric density using four different empirical models CIRA86 (Hedin et al., 1988), NRLMSISE-00 (Picone et al., 2002), DTM2013 (Bruinsma, 2015) and JB2008 (Bowman et al., 2008c). The corresponding mean values of the estimated scaling factors read 0.65 ± 0.26 for CIRA86, 0.65 ± 0.25 for NRLMSISE-00, 0.79 ± 0.24 for DTM2013 and 0.89 ± 0.27 for JB2008 and indicate that all these models clearly overestimate the thermospheric density at a period of low solar activity.

Using the same approach and models we derived 6-hour to 12-hour time series of estimated scaling factors for the thermospheric density of the CH-Therm-2018 model. Figure 7 shows these results in the comparison to the corresponding scaling factors from the JB2008 model. The median and mean values of the estimated scaling factors are 1.267 and 1.401, respectively. These values indicate that the CH-Therm-2018 model underestimates the thermospheric density at the time interval used. In fact, the underestimation of our model around August 2009 compared to CHAMP measurements is also seen from Fig. 5. The possible reason could be that the ANDE-Pollux observations we compared here are taken in August and September 2009, while the CHAMP dataset we used for constructing the CH-Therm-2018 model reaches only until the end of July 2009. The CHAMP measured thermospheric mass density increases dramatically around October 2009, when its orbit is lower than 310 km. Therefore, it is difficult to consider reliably the later period in the CH-Therm-2018 model.

5 Summary

We have derived a new model of the thermospheric neutral density, called CH-Therm-2018, from the CHAMP accelerometer measurements over 9-year period from August 2000 to July 2009, covering both high and low solar activity conditions (solar flux index P10.7 ranges from over 250 SFU to below 70 SFU). The CHAMP altitude changed from 460 km down to 310 km within this period. The comparison between our model predictions with the NRLMSISE-00 model shows that the thermospheric density predicted by the CH-Therm-2018 model agrees well (within $\pm 20\%$) with the CHAMP observations over the whole period, while the NRLMSISE-00 model overestimates the observations by about 30% and 80% at the periods of high and low solar activities, respectively. The CH-Therm-2018 model shows quite different features of the thermospheric mass density at different solar activity conditions. For example, the equatorial mass density anomaly is more prominent at higher solar activity; the larger density at the March equinox than the September equinox is only seen at higher solar activity, while this seasonal asymmetry exhibits an opposite sense during lower solar activity conditions; at low and equatorial latitudes the thermospheric mass density presents mainly longitudinal wave-4 and wave-3 patterns at higher solar activity, changing to wave-3 and wave-2 at lower solar activity.

An independent validation of the model-predicted mass densities by comparing with the density estimates derived from SLR observations of the spherical satellite ANDE-Pollux, obtained during the period of low solar activity (August 16 to September 30, 2009), reveals that the density values of the CH-Therm-2018 model should be upscaled by a factor of 1.267 ± 0.597 to fit the SLR observations.

Competing interests. The authors declare that they have no conflict of interest.

Acknowledgements. The CHAMP mission was sponsored by the Space Agency of the German Aerospace Center (DLR) through funds of the Federal Ministry of Economics and Technology. The CHAMP thermospheric mass density data are available at the website of air density models derived from multi-satellite drag observations (http://thermosphere.tudelft.nl/acceldrag/data.php). This work was supported by the

5 Priority Program 1788 "Dynamic Earth" of the German Research Foundation (DFG), through the project "Interactions of Low-Orbiting Satellites With the Surrounding Ionosphere and Thermosphere (INSIGHT)".

References

Bowman, B.R., W.K. Tobiska, F.A. Marcos, C. Valladares (2008a) The JB2006 empirical thermospheric density model. J Atmos Sol-Terr Phys, vol 70 (2008), pp. 774-793.

Bowman B.R., W.K. Tobiska, F.A. Marcos, C.Y. Huang, C.S. Lin, W.J. Burke (2008) A new empirical thermospheric density model JB2008 using new solar and geomagnetic indices. AIAA/AAS Astrodynamics Specialist Conference and Exhibit, AIAA 2008-6438.

Bruinsma, S.L., G. Thuillier, F. Barlier (2003),The DTM-2000 empirical thermosphere model with new data assimilation and constraints at lower boundary: accuracy and properties. J Atmos Sol-Terr Phys, 65, pp. 1053-1070.

Bruinsma, S. L., and J. M. Forbes (2010), Anomalous behavior of the thermosphere during solar minimum observed by CHAMP and GRACE, J. Geophys. Res., 115, A11323, doi:10.1029/2010JA015605.

Bruinsma, S.L., E. Doornbos, B.R. Bowman (2012) Validation of GOCE densities and evaluation of thermosphere models. Adv Space Res., 54 (2014), pp. 576-585.

Bruinsma, S.L. (2015) The DTM-2013 thermosphere model. J Space Weather and Space Climate, 5, A1, doi: 10.1051/swsc/2015001.

Champion, K.S.W., F.A. Marcos (1973) The triaxial-accelerometer system on atmosphere explorer. Radio Sci, 8 (1973), pp. 297-303.

Christensen, A.B., et al. (2003) Initial observations with the Global Ultraviolet Imager (GUVI) in the NASA TIMED satellite mission. J Geophys Res, 108, 1451, doi: 10.1029/2003JA009918, A12.

Clemmons, J.H., J.H. Hecht, D.R. Salem, and D.J. Strickland (2008) Thermospheric density in the Earth's magnetic cusp as observed by the Streak mission. Geophys Res Lett, 35, L24103, doi: 10.1029/2008GL035972.

Doornbos, E., J. Van Den Ijssel, H. Lühr, M. Förster, G. Koppenwallner (2010) Neutral density and crosswind determination from arbitrarily oriented multiaxis accelerometers on satellites. J Spacecraft Rockets, 47, pp. 580-589.

Emmert, J.T., J.M. Picone, J.L. Lean, S.H. Knowles (2004) Global change in the thermosphere: Compelling evidence of a secular decrease in density. J Geophys Res - Space Phys, 109(A2), doi: 10.1029/2003JA010176

Emmert, J.T. (2015) Thermospheric mass density: A review. Adv Space Res, 56(5), 773–824, doi: 10.1016/j.asr.2015.05.038.

Guo, J., W. Wan, J.M. Forbes, E. Sutton, R.S. Nerem, and S. Bruinsma (2008) Interannual and latitudinal variability of the thermosphere density annual harmonics. J Geophys Res, 113, A08301, doi: 10.1029/2008JA013056.

Hagan, M.E., and J.M. Forbes (2003), Migrating and nonmigrating semidiurnal tides in the upper atmosphere excited by tropospheric latent heat release. J Geophys Res, 108(A2), 1062, doi:10.1029/2002JA009466.

Häusler, K., H. Lühr, S. Rentz, and W. Köhler (2007), A statistical analysis of longitudinal dependences of upper thermospheric zonal winds at dip equator latitudes derived from CHAMP, J. Atmos. Solar-Terr. Phys., 69, 1419–1430, doi:10.1016/j.jastp.2007.04.004

Hedin, A.E. (1983) A Revised thermospheric model based on mass spectrometer and incoherent scatter data: MSIS-83. J Geophys Res, 88(A12), 10170–10188, doi: 10.1029/JA088iA12p10170.

Hedin, A.E., N.W. Spencer, T.L. Killeen (1988) Empirical global model of upper thermosphere winds based on Atmosphere and Dynamics Explorer satellite data. J Geophys Res, 93, 9959-9978, doi: 10.1029/JA093iA09p09959.

Hedin, A.E. (1991) Extension of the MSIS Thermosphere Model into the middle and lower atmosphere. J Geophys Res, 96(A2), 1159–1172, doi: 10.1029/90JA02125.

Immel, T.J., E. Sagawa, S.L. England, S.B. Henderson, M.E. Hagan, S.B. Mende, H.U. Frey, C.M. Swenson, and L.J. Paxton (2006), Control of equatorial ionospheric morphology by atmospheric tides, Geophys Res Lett, 33, L15108, doi:10.1029/2006GL026161.

King-Hele, D. (1987) Satellite orbits in an atmosphere. Blackie and Son Ltd., London

Lei, J., T. Matsuo, X. Dou, E. Sutton, and X. Luan (2012) Annual and semiannual variations of thermospheric density: EOF analysis of CHAMP and GRACE data. J Geophys Res, 117, A01310, doi: 10.1029/2011JA017324.

Liu, H., H. Lühr, V. Henize, and W. Köhler (2005) Global distribution of the thermospheric total mass density derived from CHAMP. J Geophys Res, 110, A04301, doi: 10.1029/2004JA010741.

Liu, H., H. Lühr, S. Watanabe, W. Köhler, V. Henize, and P. Visser (2006) Zonal winds in the equatorial upper thermosphere: Decomposing the solar flux, geomagnetic activity, and seasonal dependencies. J Geophys Res, 111, A09S29, doi: 10.1029/2005JA011415.

Liu, H., H. Lühr, and S. Watanabe (2007) Climatology of the equatorial mass density anomaly. J Geophys Res, 112, A05305, doi: 10.1029/2006JA012199.

Liu, H., M. Yamamoto, and H. Lühr (2009b), Wave-4 pattern of the equatorial mass density anomaly—A thermospheric signature of tropical deep convection, Geophys. Res. Lett., 36, L18104, doi:10.1029/2009GL039865.

Liu, R., H. Lühr, E. Doornbos, and S.-Y. Ma (2010) Thermospheric mass density variations during geomagnetic storms and a prediction model based on the merging electric field. Ann Geophys, 28, 1633–1645, doi: 10.5194/angeo-28-1633-2010.

Liu, R., Ma, S.-Y., and Lühr, H. (2011) Predicting storm-time thermospheric mass density variations at CHAMP and GRACE altitudes. Ann Geophys, 29, 443-453, doi: 10.5194/angeo-29-443-2011.

Liu, H., T. Hirano, and S. Watanabe (2013) Empirical model of the thermospheric mass density based on CHAMP satellite observation. J Geophys Res Space Physics, 118, 843–848, doi: 10.1002/jgra.50144.

Liu, X., J.P. Thayer, A. Burns, W. Wang, and E. Sutton (2014a) Altitude variations in the thermosphere mass density response to geomagnetic activity during the recent solar minimum. J Geophys Res Space Physics, 119, 2160–2177, doi: 10.1002/2013JA019453.

Lühr, H., M. Rother, W. Köhler, P. Ritter, and L. Grunwaldt (2004) Thermospheric up-welling in the cusp region: Evidence from CHAMP observations. Geophys Res Lett, 31, L06805, doi: 10.1029/2003GL019314.

Lühr, H., M. Rother, K. Häusler, P. Alken, and S. Maus (2008), The influence of non-migrating tides on the longitudinal variation of the equatorial electrojet, Geophys Res Lett, 113, A08313, doi:10.1029/2008JA013064.

Marinov, P.G., I.S. Kutiev, and S. Watanabe (2004) Empirical model of O+ - H+ transition height based on topside sounder data. Adv Space Res, 34, 2021-2025, doi: 10.1016/j.asr.2004.07.012.

Meier, R.R., and J.M. Picone (1994) Retrieval of absolute thermospheric concentrations from the far UV dayglow: An application of discrete inverse theory. J Geophys Res, 99(A4), 6307–6320, doi: 10.1029/93JA02775.

Newell, P.T., T. Sotirelis, K. Liou, C.-I. Meng, F.J. Rich (2007) A nearly universal solar wind-magnetosphere coupling function inferred from 10 magnetospheric state variables. J Geophys Res - Space Phys, 112(A1), doi: 10.1029/2006JA012015

Osborne, J.J., I.L. Harris, G.T. Roberts, A.R. Chambers (2001) Satellite and rocket-borne atomic oxygen sensor techniques. Rev Sci Instrum, 72, pp. 4025-4041.

Panzetta F., Bloßfeld M., Erdogan E., Rudenko S., Schmidt M., Müller H.: Towards thermospheric density estimation from SLR observations of LEO satellites - A case study with ANDE-Pollux satellite, J. Geodesy, submitted, under review.

Picone, J.M., A.E. Hedin, D.P. Drob, and A.C. Aikin (2002) NRLMSISE-00 empirical model of the atmosphere: Statistical comparisons and scientific issues. J Geophys Res, 107(A12), 1468, doi: 10.1029/2002JA009430.

Reigber, C., H. Lühr, and P. Schwintzer (2002) CHAMP mission status, Adv. Space Res., 30, 129–134.

Tapley, B.D., Bettadpur, S., Watkins, M., et al. (2004), The gravity recovery and climate experiment: mission overview and early results. Geophys. Res. Lett., 31, L09607.

Thayer, J.P., X. Liu, J. Lei, M. Pilinski, and A.G. Burns (2012), The impact of helium on thermosphere mass density response to geomagnetic activity during the recent solar minimum. J Geophys Res, 117, A07315, doi: 10.1029/2012JA017832.

The Rocket Panel (1952) Pressures, densities, and temperatures in the upper atmosphere. Phys Rev, 88, pp. 1027-1032.

Von Zahn, U. (1970) Neutral air density and composition at 150 kilometers. J Geophys Res, 75(28), 5517–5527, doi: 10.1029/JA075i028p05517.

Wan, W., J. Xiong, Z. Ren, L. Liu, M.-L. Zhang, F. Ding, B. Ning, B. Zhao, and X. Yue (2010), Correlation between the ionospheric WN4 signature and the upper atmospheric DE3 tide, J. Geophys. Res., 115, A11303, doi:10.1029/2010JA015527.

Werner S., and G.W. Prölss (1997) The position of the ionospheric trough as a function of local time and magnetic activity. Adv Space Res, 20(9), pp. 1717-1722, doi: 10.1016/S0273-1177(97)00578-4

Xiong, C., and H. Lühr (2014) An empirical model of the auroral oval derived from CHAMP field-aligned current signatures-Part 2. Ann Geophys, 32, 623–631, doi: 10.5194/angeo-32-623-2014.

Xiong, C., H. Lühr, and B.G. Fejer (2016) The response of equatorial electrojet, vertical plasma drift, and thermospheric zonal wind to enhanced solar wind input. J Geophys Res Space Physics, 121, 5653–5663, doi: 10.1002/2015JA022133.

Yamazaki, Y., M.J. Kosch, and E.K. Sutton (2015) A model of high-latitude thermospheric density. J Geophys Res Space Physics, 120, 7903–7917, doi: 10.1002/2015JA021371.

Zhou, Y.L., Ma, S.Y., Liu, R.S., Luehr, H., and Doornbos, E. (2013) Controlling of merging electric field and IMF magnitude on storm-time changes in thermospheric mass density. Ann Geophys, 31, 15-30, doi: 10.5194/angeo-31-15-2013.

Table 1. The derived values of parameters as defined in Eqs. (4) to (10) for constructing the CH-Therm-2018 empirical model.

Parameters	Coefficients	2000.08-2005.07	2004.08-2009.07
h	ρ_0	1.02478 e−01	7.66390 e−02
	H_d	9.43487 e+01	7.99404 e+01
P10.7	a_0	2.20442 e+01	1.64789 e+01
	a_1	2.07964 e−01	3.43898 e−01
	a_2	−4.90736 e−05	−1.60896 e−03
DoY	b_0	1.0	1.0
	b_{11}	2.09135 e−01	1.31082 e−01
	b_{12}	−1.33610 e−01	−1.18733 e−01
	b_{13}	−2.31834 e−03	−4.08388 e−02
	b_{21}	9.57844 e−02	2.19884 e−02
	b_{22}	−4.43634 e−02	−5.93100 e−02
	b_{23}	3.25542 e−02	−1.37226 e−02
MLT	c_0	1.0	1.0
	c_{11}	−2.78983 e−01	−2.77790 e−01
	c_{12}	2.84595 e−02	3.92145 e−02
	c_{13}	−4.49755 e−03	−7.25256 e−04
	c_{14}	−9.69936 e−03	1.52304 e−02
	c_{21}	−1.98421 e−01	−2.17354 e−01
	c_{22}	4.30628 e−02	4.59899 e−02
	c_{23}	−9.29224 e−03	4.73289 e−03
	c_{24}	−2.95443 e−03	1.23554 e−02
Θ	d_0	1.0	1.0
	d_{11}	1.09347 e−01	1.44814 e−01
	d_{12}	−1.29948 e−02	7.29394 e−03
	d_{13}	−8.31644 e−03	−6.45977 e−03
	d_{14}	−3.59449 e−03	−1.14291 e−03
	d_{15}	5.22521 e−04	−5.87996 e−04
	d_{16}	−1.10054 e−03	2.19460 e−04
	d_{21}	1.01188 e−02	5.78031 e−02
	d_{22}	2.34080 e−03	−1.82840 e−02
	d_{23}	−9.32401 e−04	1.23597 e−02
	d_{24}	−1.72102 e−03	−1.22364 e−02
	d_{25}	−1.56578 e−03	7.92947 e−03
	d_{26}	1.41373 e−03	−6.42885 e−03
ϕ	g_0	1.0	1.0
	g_{11}	−4.77705 e−03	−2.64432 e−03
	g_{12}	−1.47749 e−03	−2.63336 e−03
	g_{13}	1.51963 e−03	3.21108 e−03
	g_{14}	1.65757 e−04	−1.80075 e−03
	g_{21}	−5.66262 e−03	−5.37701 e−03
	g_{22}	3.01145 e−03	−1.33626 e−03
	g_{23}	6.08981 e−05	1.21844 e−03
	g_{24}	9.34866 e−05	2.79883 e−05
E_m	m_0	3.59143 e+00	2.66925 e+00
	m_1	1.67998 e−01	3.16646 e−01
	m_2	1.20592 e−03	−3.65431 e−03
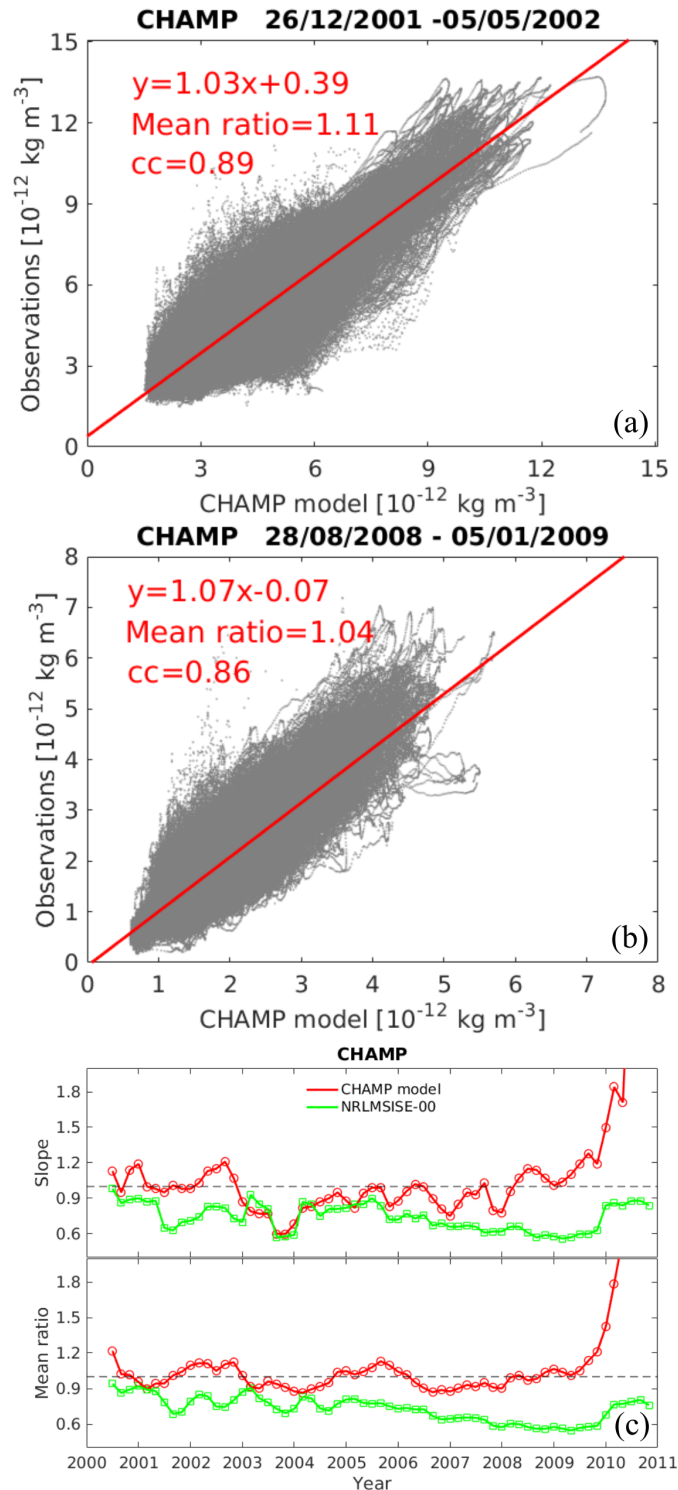
Figure 6. The linear regression between the CHAMP observations and the model-predicted results during 131-day period (a) for high (centered on March 1, 2002) and (b) low (centered on November 1, 2008) solar activity conditions, respectively. (c) The red color shows the slope (top panel) and mean ratio (bottom panel) of the linear regression for each 2-month period from 2000 to 2010. The green color shows the results from NRLMSISE-00 model.
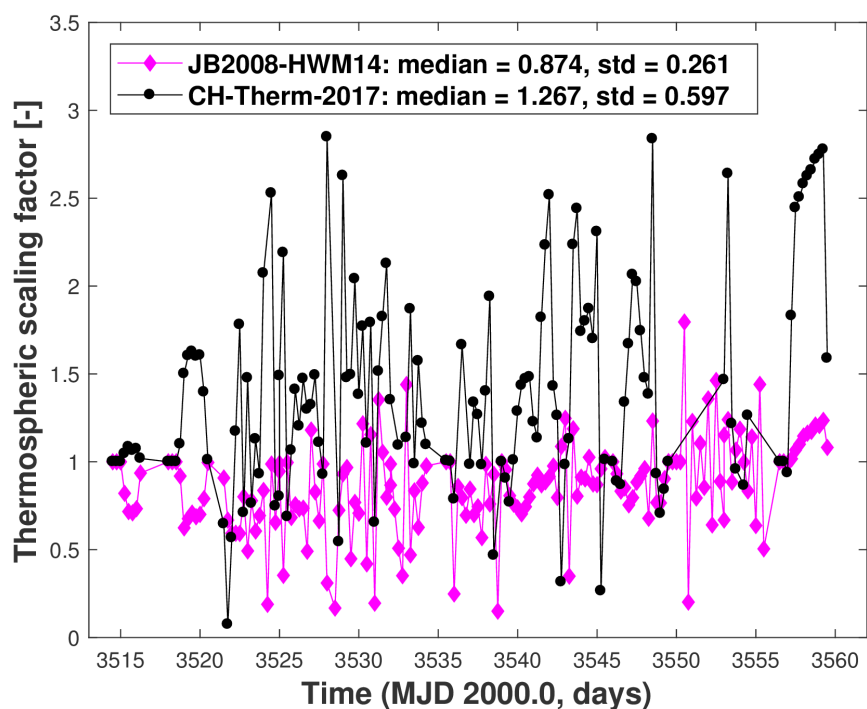
Figure 7. Scaling factors of thermospheric density derived from the analysis of SLR data of ANDE-Pollux from August 16 to September 30, 2009 for two models: JB2008 and CH-Therm-2018.